

ASPCNet: A Deep Adaptive Spatial Pattern Capsule Network for Hyperspectral Image Classification

Jinping Wang[✉], *Student Member, IEEE*, Xiaojun Tan[✉],
Jianhuang Lai[✉], *Senior Member, IEEE*, Jun Li[✉], and Canqun Xiang

Abstract—Previous studies have shown the great potential of capsule networks for the spatial contextual feature extraction from hyperspectral images (HSIs). However, the sampling locations of the convolutional kernels of capsules are fixed and cannot be adaptively changed according to the inconsistent semantic information of HSIs. Based on this observation, this paper proposes an adaptive spatial pattern capsule network (ASPCNet) architecture by developing an adaptive spatial pattern (ASP) unit, that can rotate the sampling location of convolutional kernels on the basis of an enlarged receptive field. Note that this unit can learn more discriminative representations of HSIs with fewer parameters. Specifically, two cascaded ASP-based convolution operations (ASPConvs) are applied to input images to learn relatively high-level semantic features, transmitting hierarchical structures among capsules more accurately than the use of the most fundamental features. Furthermore, the semantic features are fed into ASP-based conv-capsule operations (ASPCaps) to explore the shapes of objects among the capsules in an adaptive manner, further exploring the potential of capsule networks. Finally, the class labels of image patches centered on test samples can be determined according to the fully connected capsule layer. Experiments on three public datasets demonstrate that ASPCNet can yield competitive performance with higher accuracies than state-of-the-art methods.

Index Terms—Capsule networks, adaptive spatial pattern neural network, hyperspectral image classification

I. INTRODUCTION

HYPERSPECTRAL remote sensing technology has attracted much attention in recent years since it can include hundreds of contiguous spectral bands and capture more accurate and discriminative features for different objects, especially compared with panchromatic and multi-spectral images. Hyperspectral image classification (HSIC), which refers to automatically assigning a specific label for each pixel in a scene, has become an active topic in many research fields,

such as defense and security [1], intelligent transportation, intelligent healthcare [2], [3], and forest and unmanned aerial vehicle monitoring (e.g., mangrove biomass estimation) [4], [5].

During the last few decades, a large number of pixelwise-based classifiers, mainly based on spectral signatures, have been proposed for classification tasks, such as support vector machines (SVMs) [6], logistic regression [7], k -nearest-neighbors [8], [9], and random forests [10], [11]. With the improvement in sensor spatial resolution, many spectral-spatial-based classification methods play roles [12]–[18], taking the spatial information of images into consideration and improving the classification accuracies. As one of the crucial steps in spectral-spatial classification, feature extraction-based methods have attracted much attention. Some state-of-the-art feature extraction methods, which are mainly based on general machine learning techniques, have achieved good classification performance, such as the image fusion and recursive filtering [19] method, the extended morphological profiles (EMP) [20] method, the edge-preserving filter (EPF) [21] method, and the superpixel segmentation method [22], [23]. However, the aforementioned feature extraction approaches mainly classify an image in a shallow manner, e.g., the feature extractors and classifiers only focus on a single layer. Comparatively, deep learning-based techniques can allow computers to learn different image features through a series of hierarchical layers, and the learning process is totally automatic and efficient. Currently, deep network models are widely used in many image processing tasks [24]–[28]. Typical deep learning networks for HSIC can be summarized into five categories [29]: stacked autoencoders [30], [31], deep belief networks [32], recurrent neural networks [33], generative adversarial networks [34], and convolutional neural networks (CNNs) [35].

Unlike other deep learning methods, CNN models possess local receptive fields and shared weight architecture, and have shown strong abilities in the feature extraction process. Generally, CNNs can be grouped into two classes: (1) The first class extracts spectral-spatial characteristics by simultaneously using 3D filtering. As the layers go deeper, the model features become more precise and reliable [36], [37]. Considering that the pooling operation of CNNs may lose the spatial information of hyperspectral images (HSIs), the dilated neural networks were introduced for HSIC [38]–[40], and the core idea of which is to avoid resolution reduction in the pooling layer while enlarging the receptive field through a dilated convolution strategy. Moreover, a multi-scale dilated residual CNN has been proposed to improve further classification

This work was supported by the Key-Area Research and Development Program of Guangdong Province under Grant 2020B090921003 and Southern Marine Science and Engineering Guangdong Laboratory (Zhuhai) under Grant SML2020SP011. (Corresponding author: Jun Li.)

J. Wang, X. Tan, and J. Li are with the School of Intelligent Systems Engineering, Sun Yat-sen University, Guangzhou, 510006, China (e-mail: wangjp29@mail2.sysu.edu.cn; tanxj@mail.sysu.edu.cn; stslj@mail.sysu.edu.cn).

J. Lai is with the School of Computer Science and Engineering, Sun Yat-sen University, and also with the Key Laboratory of Machine Intelligence and Advanced Computing, Ministry of Education, Sun Yat-sen University, Guangzhou, 510006, China (e-mail: stsljh@mail.sysu.edu.cn).

J. Wang and X. Tan are with Southern Marine Science and Engineering Guangdong Laboratory (Zhuhai), Zhuhai, 519082, China.

C. Xiang is with the College of Electronics and Information Engineering, Shenzhen University, Shenzhen 518060, China (e-mail: xiangcanqun2018@email.szu.edu.cn)

performance [41]. (2) The second class extracts the spectral and spatial characteristics and subsequently fuses them. In the literature [42], a spectral-spatial fully convolutional network is proposed that introduces a dense conditional random field into two parallel flows to balance the obtained spectral and spatial features. In contrast, Li *et al.* used a fusion scheme with layer-specific regularization and smooth normalization to adaptively learn the fusion weights of local and global information [43]. Moreover, the fusion of multilevel and multiscale-based spatial-spectral CNNs also has potential for HSI [44], [45].

Although general CNNs are capable of image feature extraction, some shortcomings still exist that strongly threaten the performance of deep learning methods, such as problems related to the loss of local information caused by the pooling layer and an inability to understand spatial positional relationships among features. To overcome these issues, Sabour *et al.* proposed a capsule network (CapsuleNet) [46] that can achieve results superior to those of CNNs. Later, capsulenet was first introduced for HSIC in [47]. However, the original capsulenet includes only one convolution layer and one fully connected capsule layer. To deepen the method and allow it to solve problems due to the stacking of multicapsule layers, many capsulenet-based expansions have been proposed that can achieve better classification performance [48]–[52]. Motivated by the core ideas of CNNs, a modification of the traditional capsulenet named conv-capsule has been proposed for classification [50], [51], which uses a conv-capsule unit to achieve a local connection and shared transform matrices. Experimental results indicate that the conv-capsule unit provides results competitive with those of traditional capsulenet. Moreover, Xu *et al.* designed multiple kernels with parallel convolution to extract image features in a multi-scale way, reducing the redundancy of parameters and achieving high accuracies for HSIC [52]. These works have demonstrated the excellent performance of capsulenet.

However, there are still some shortcomings in the existing capsulenets. First, the semantic features fed into primarycaps are extracted by a simple convolutional layer, which may not be efficient in representing and transferring hierarchical structures among capsules, compared with relatively high-level semantic features. Second, although the 3D conv-capsulenet uses local connections and shared weights to fully use the spectral-spatial information, the window size is fixed and cannot be adjusted according to the different shapes of input images. Third, the traditional neural networks use pooling layers to enlarge the receptive field while reducing the model complexity. However, some detailed features might disappear after several pooling operations. To overcome these defects, a novel adaptive spatial pattern capsule network (ASPCNet) has been proposed that consists of the following major steps:

First, relatively high-level features obtained by adaptive spatial pattern convolution operations (ASPConvs) are fed into primarycaps. Next, adaptive spatial pattern-based conv-capsule operations (ASPCaps) are proposed during the dynamic routing process, adaptively adjusting the convolutional kernel sampling locations. Finally, the class label of pixels can be determined according to the fully connected capsule layer. The contributions of this paper are described as follows:

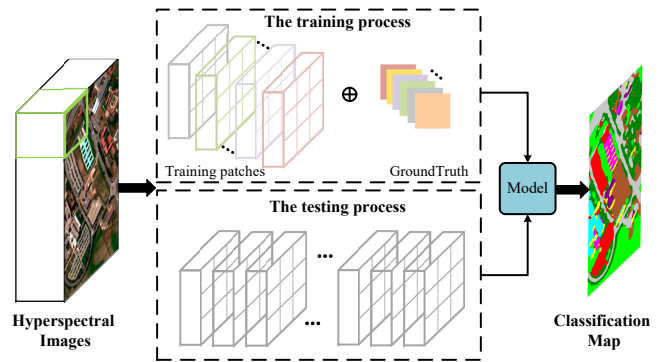


Fig. 1. The architecture of the supervised learning-based classification of hyperspectral images.

1) A novel adaptive spatial pattern (ASP) unit is constructed by adaptively rotating the sampling location on the basis of dilated convolutions. Instead of using the downsampling strategy, the cascaded ASP layers can simultaneously expand the receptive field and avoid checkerboard effects.

2) A series of ASPConvs are used for feature extraction before the primarycaps layer. The obtained relatively high-level semantic features can offer better services for hierarchical relationship representation among capsules regarding the transmission efficiency and representation ability.

3) ASPCaps is developed into a dynamic routing process that can adaptively adjust the shape of local connections according to HSI's complex spatial contexts to ensure that the model has a strong generalization ability.

4) Experiments conducted on several real hyperspectral datasets demonstrate that the proposed ASPCNet can always obtain better results and more accurate classification maps than state-of-the-art methods.

The remainder of this paper is organized as follows. Section II describes the related works. Section III presents the details of the proposed ASPCNet approach. In Section IV, the experimental results and discussions are provided. Finally, conclusions are given in Section V.

II. RELATED WORKS

A. CNN

CNNs, typical supervised learning methods, use image patches centered on labeled pixels as the training patches for a model training and then the well-trained model can be used for HSIC; see Fig. 1. Unlike other tools that learn manually designed features, a CNN classifier can learn different types of natural features through a stack of layers [53]–[55] that includes convolutional layers, pooling layers, and fully connected layers. In a CNN model, there are a series of fixed boxes named convolution kernels that share the weights of the network to simulate 3-D convolutional operations, and these replicated weights can significantly reduce the number of parameters in its network. The different convolution kernels slide over an input image and can transform this image into another feature domain for effectively modeling these visual features.

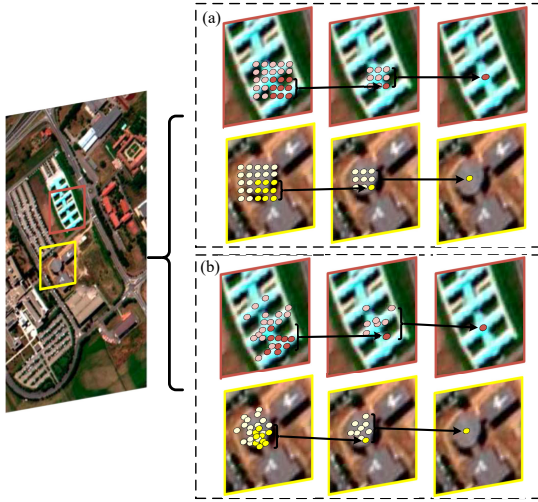


Fig. 2. Illustration of the differences between different sampling locations on the University of Pavia dataset. (a) Sampling locations based on regular convolution and (b) Sampling locations based on deformable convolution.

Specifically, we assume that the input image patches (centered on labeled pixels) are of size $N \times N \times C$. In the convolution layers, k_1 different filter kernels with windows sizes of $n \times n$ spatially slide over the image patches, obtaining a 3-D tensor of feature maps of size $M \times M \times k_1$. In addition to multiple convolutions, considering the increasing computational burden, the CNN-based model subsequently employs pooling layers to conduct feature downsampling operations for learning the hierarchy of those different features. After convolutional and pooling layers are achieved, the fully connected layers stack the output values of all previous layers into an n -dimensional vector. After a series of fully connected layers, the softmax layer is used to generate the distribution of the probability that the pixel belongs to each class.

B. DCNN

CNNs are successful models that can effectively extract the detailed features of input images and assign a specific class label for each particular pixel. Suppose the receptive fields of a traditional convolution are of size $N \times N$, and given a pixel a , suppose the image location of a is (x, y) , and its corresponding value is $p(x, y)$. The output form of centered pixel a can be obtained as follows

$$O(x, y) = \sum_{(x_n, y_n) \in s} \omega(x_n, y_n) \cdot p(x + x_n, y + y_n), \quad (1)$$

where $s = (x, y) \mid (0, 0), (0, 1), \dots, (N-1, N-1)$, which enumerates the location of the kernel and ω represents the weight of the kernel.

However, considering that the spatial shapes and locations of convolutional operations $N \times N$ are fixed, which is not suitable for representing complex image features, deformable convolution neural networks (DCNNs) were conceived in the computer vision field to overcome the problem [56], [57]. Later, the ideal of deformable neural networks was introduced into HSI [58], which can effectively extract HSI features, especially for its complex spatial structures. As we can see

from Fig. 2, there is a contrast between the sampling locations of regular convolution and sampling locations of deformable convolution, in which the deformable convolution is present in the shapes of a rhombus and a circle, showing better coverage. Specifically, two values Δx , and Δy are introduced into the offset field. In this way, the output form of centered a can be changed as follows:

$$O(x, y) = \sum_{(x_n, y_n) \in s} \omega(x_n, y_n) \cdot p(x + x_n + \Delta x, y + y_n + \Delta y). \quad (2)$$

However, Δx and Δy are fractional locations, and they cannot directly obtain the real locations. Thus, to avoid checkerboard artifacts, bilinear interpolation is used to obtain these values. The value of $p(\Delta x, \Delta y)$ is calculated according to the values of the four surrounding integer locations. The weights of the convolutional filters for generating offset fields are trained based on spatial features to enable the sampling locations to be transferred to similar neighboring pixels.

C. CapsuleNet

In capsulenet, specific types of functional neurons are grouped together to form capsules, and individual neurons represent one of various attributes of a specific entity in an image. A capsulenet can discriminate the consistency of the contextual information of the capsules and therefore has a better ability to model the spatial positions of visual features of images than a CNN. Due to their advantages, capsulenet have been widely used in many image processing tasks, such as face recognition, optical character recognition, and scene classification [59], [60].

In a capsulenet, the steps for transformation from the output active vector u_i of the shallow feature layer to the output active vector v_j of the high feature layer are as follows:

First, the u_i of the previous capsule is multiplied by a weighted matrix W_{ij} , and then the prediction vector $u_{j|i}$ can be obtained by

$$u_{j|i} = W_{ij}u_i, \quad (3)$$

where u_i represents the i th feature in the shallow layer, and $u_{j|i}$ is its j th prediction feature in the high feature layer. Then, s_j in capsule j is obtained as a weighted sum of all the prediction vectors $u_{j|i}$ from the shallow layer.

$$s_j = \sum_i c_{ij}u_{j|i}, \quad (4)$$

where c_{ij} denotes the coupling coefficient, which is determined by a routing softmax processing of dynamic routing [46], and s_j is the input vector of capsule j . Finally, capsule j uses the length of s_j to determine the probability of the existence of the entity; therefore, a nonlinear function called squash function is used to squash vector s_j as follows

$$v_j = \frac{\|s_j\|^2}{1 + \|s_j\|^2} \frac{s_j}{\|s_j\|}, \quad (5)$$

where v_j represents the output of capsule j , which can be considered a vector representation of the input. Through the capsulenet, a more robust extracted feature representation of the input image patch can be obtained. Later, the probability

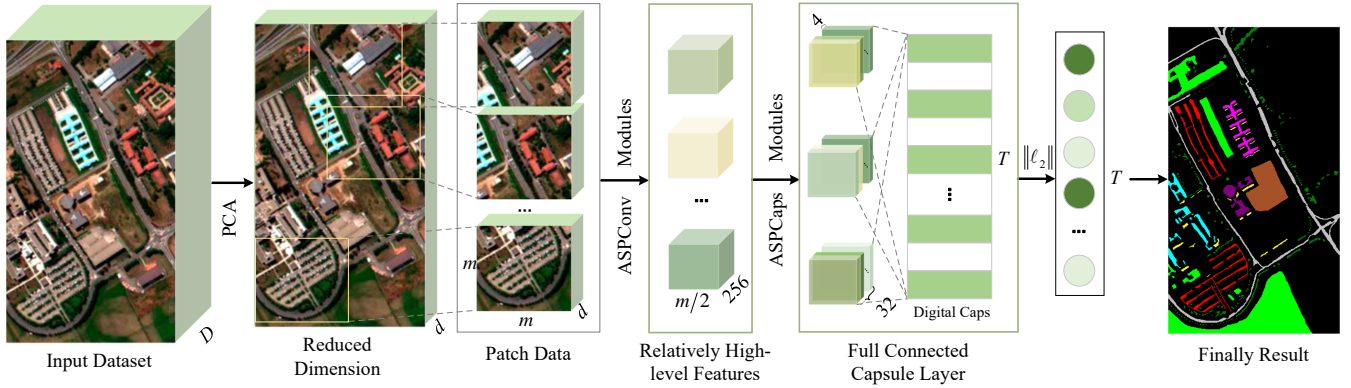


Fig. 3. The framework of the proposed ASPCNet for HSIC.

of the entity can be determined by calculating the length of the activity vector.

III. THE PROPOSED APPROACH

Assume an input HSI \mathbf{X} with the size of $H \times W \times D$, and $\mathbf{X} \in \mathbb{R}^{H \times W \times D}$. Each training pixel $\mathbf{X}^k \in \mathbb{R}^{1 \times 1 \times D}$, $k = 1, 2, \dots, K$, where D and K represent the dimension of HSI and the number of training samples, respectively. Suppose that T represents the total class in HSI. For each pixel \mathbf{X}^k , the truth label of \mathbf{X}^k can be represented as \mathbf{t}^k , which is actually a vector of length t with value “1” at the position of the correct label and “0” elsewhere. Different from the natural image classification, which inputs whole images, the HSI classification based on CNN uses image patches centered on labeled pixels as the input samples. Here, we conduct a standard preprocessing step, i.e., the principal component analysis (PCA) algorithm, for HSI dimension reduction. Therefore, HSI’s band channels shrink from D to d . Let $\mathbf{X}^k \in \mathbb{R}^{1 \times 1 \times d}$ be the center pixel of dimension reduction images, the image patch can be represented as $\mathbf{Y}^k \in \mathbb{R}^{m \times m \times d}$ of the window size $m \times m$, and $\{\mathbf{Y}^k, \mathbf{t}^k\}_{k=1}^K$ represents the input samples. Since the ASP units are the core components of the proposed ASPCNet, in Section III-A, we first give a detailed description of the ASP unit and ASP-based convolution operation (ASPConvs) in the task of HSIC. Then, we develop the ASP unit into the process of the original capsulenet (ASPCaps) in Section III-B. Finally, the overall architecture of the proposed ASPCNet is given in Section III-C and Fig. II-B.

A. ASPConvs

Given an image patch (centered on labeled pixel) $\mathbf{Y}^k \in \mathbb{R}^{m \times m \times d}$ with a window size of $m \times m$, the sampling locations of the input image can be represented as $s_1 = \{(0, 0), (0, 1), \dots, (m-1, m-1)\}$. The traditional convolution operation consists of two steps: 1) sampling using a series of regular grids \mathfrak{R} of size $p \times q$ slide over the input image patch and 2) the summation of sampled values weighted by \mathbf{W} for different convolution kernels. A larger size of regular grids \mathfrak{R} can be replaced by multiple smaller sizes of \mathfrak{R} with the same receptive field. As the convolution network model goes deeper, the pooling layers are supposed to shrink the

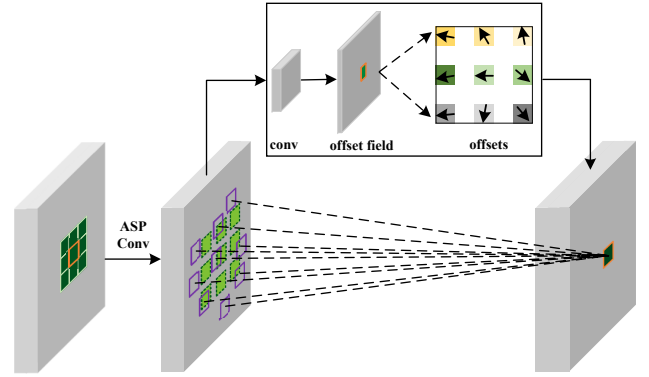


Fig. 4. Illustration of the process of the ASPConv module. The pixel marked by the orange box is the central pixel. After ASPConv is applied to the input images, the sampling locations of regular convolutional filters can be transferred to the pixels in the purple boxes.

model’s parameters. Unfortunately, the principle behind the pooling operation is to preserve distinctive and representative features of each pooling area. This means that some details tend to disappear after several pooling operations, which is extremely unfavorable for classification accuracy. In addition, the sampling locations of the general convolution layer are fixed; this configuration cannot effectively extract the spatial information according to the different structures of input image patches. Therefore, to overcome these issues, the ASP unit is proposed in this paper, which simultaneously expands the receptive field and rotates the sampling location, i.e., integrating dilated and deformation operations into one unit (see Fig. 4). The details are shown as follows:

First, we can introduce the dilated convolution to implement the larger receptive field with fewer parameters. For instance, two 3×3 filters along with a 2-dilation rate can be equally replaced by one 9×9 filter with a 1-dilation rate, which can prevent the loss of the spatial relative relationship of pixels caused by the downsampling operation. Grid \mathfrak{R}' defines the locations of the modified dilated convolution kernels, which are described below. Suppose the dilation rate $h_{dr}=3$, $\mathfrak{R}' = \{(x, y) | (-3, -3), (-3, -1), \dots, (1, 3), (3, 3)\}$. Here, h_{dr} can be changed freely in this model according to the different shapes of images; its effect is analyzed in Section IV-D3. For

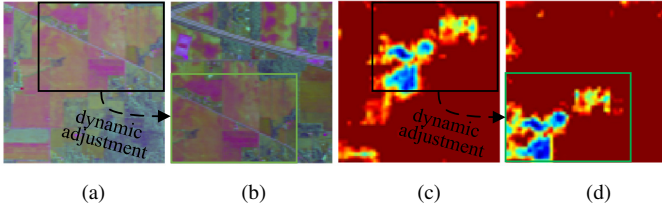


Fig. 5. Two image patches with the same region of interest. (a) and (b) Pseudo color images and (c) and (d) Visualization features of contributing scores. Different colors indicate the proportion of contribution in the feature learning process, where blue indicates higher contribution scores and red indicates lower contribution scores.

any dilation rate h_{dr} , its size can be calculated as

$$p_{dr} = p + (p - 1)(h_{dr} - 1), \quad (6)$$

$$q_{dr} = q + (q - 1)(h_{dr} - 1), \quad (7)$$

where p_{dr} and q_{dr} refer to the height and width of a kernel of dilated convolution, respectively. There are only no more than $p \times q$ nonzero values in a $p_{dr} \times q_{dr}$ area.

However, without a brilliantly designed dilated convolution structure [61], multiple cascaded dilated convolutional layers result in a gridding effect while hurting the continuity of the kernel due to the checkerboard processing method. Based on this observation, a deformable convolution operation is combined with dilated convolution to adaptively adjust the sampling location of the grid kernel. Therefore, the new unit called the ASP unit is promoted, which can directly choose the grid location in an adaptive way to search for the most relevant pixels in a local area and achieve a larger receptive field, fewer parameters, and more spatial information.

Specifically, given one location (x, y) of the grid \mathcal{R}' and its value $\mathcal{R}'(x, y)$ which corresponds to two values $\Delta x, \Delta y$ in the offset field. In this way, the adaptive spatial unit is generated to fuse the information of similar neighboring pixels, which can be obtained by

$$\mathcal{R}'_{\text{new}}(x, y) = \mathbf{Y}^k(\mathcal{R}'(x, y) + (\Delta x, \Delta y)) = \mathcal{R}'(x', y'), \quad (8)$$

where x' and y' refer to fractional locations and can be represented as $x' = \min(\max(0, x + \Delta x), p - 1)$, and $y' = \min(\max(0, y + \Delta y), q - 1)$. The value of $\mathcal{R}'(x', y')$ is calculated according to the values of the surrounding integer locations via bilinear interpolation.

Finally, the adaptive spatial feature $\mathbf{u}(x, y)$ of location (x, y) can be extracted as follows

$$\mathbf{u}(x, y) = \sum_{i=1}^{\text{Len}(\mathcal{R}')} w_i \cdot \mathcal{R}'_{\text{new}}(x_i, y_i) \cdot \Delta m_i, \quad (9)$$

where w_i represents the corresponding weight of the kernel. Δm_i refers to the weight of the i th sampling pixel, and if the sample pixel does not meet the sampling rules, Δm_i tends toward zero [57]. $\text{Len}(\cdot)$ represents the length of the vector \mathcal{R}' . We provide a visual explanation of the proposed ASPConv module via gradient guided back-propagation in Fig. III-A. Focusing on the framed area, we can draw the conclusion that the proposed method can always adjust the shapes of the region of interest in adaptive rules according to the real

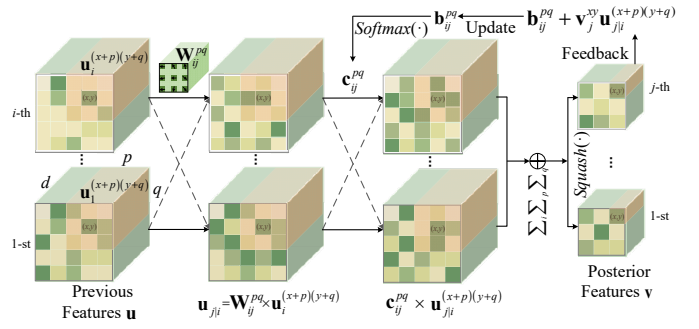


Fig. 6. Illustration of the process of the ASPCaps module, which vividly describes the transfer process from previous features \mathbf{u} to posterior features \mathbf{v} .

objects. We also package the ASP unit into a simple and easy-to-use network layer that can replace the traditional convolutional layer and can be placed anywhere.

B. ASPCaps

To create a deep and robust capsulenet with fewer parameters, there are some considerations: 1) Some robust capsule layers should be stacked. 2) Location connections and shared routing matrices should be added to a dynamic routing algorithm. 3) More adaptive spatial information should be learned through the location connection. Based on these considerations, we develop a novel deep capsulenet named ASPCNet with a special ASP unit. Specifically, an ASP-based conv-capsule named ASPCaps is introduced during the dynamic routing process to replace the general conventional convolution layer. The detailed description is shown below.

After the ASPConvs module operation, the relatively high-level features \mathbf{u} can be obtained as the input features to transfer into the primarycaps layer. The ASPCaps operation has the ability to explore the relationship among capsules. Fig. 6 shows an illustration of the ASPCaps operation. Here, we divide the previous layer feature \mathbf{u} into multiple capsules, where $\mathbf{u} = \{\mathbf{u}_i, i = 1, \dots, I\}$. Supporting the posterior layer feature \mathbf{v} with j capsules, the detailed transmission process is described in the following. For each capsule during the dynamic routing process, all the capsules in their receptive fields make a prediction through the transform matrix. Here, given a pixel at location (x, y) , $\mathbf{u}_i^{(x+p)(y+q)}$ represents the output of the capsule, which is the i -th capsule in the last capsule layer at position $(x + p, y + q)$, and \mathbf{W}_{ij}^{pq} represents the shared transform matrix between the i th capsule of layer \mathbf{u} and the j th capsule of layer \mathbf{v} , which possesses adaptive rotation rules based on ASPConv. I is the number of capsules in the last capsule layer.

$$\mathbf{u}_{j|i}^{(x+p)(y+q)} = \mathbf{W}_{ij}^{pq} \mathbf{u}_i^{(x+p)(y+q)}, \quad (10)$$

where $\mathbf{u}_{j|i}^{(x+p)(y+q)}$ denotes the j th prediction feature in the high feature layer. As all the “prediction vectors” $\mathbf{u}_{j|i}$ are obtained, the weighted sum of all capsules of $(x + p)(y + q)$ can serve as the input of the capsule.

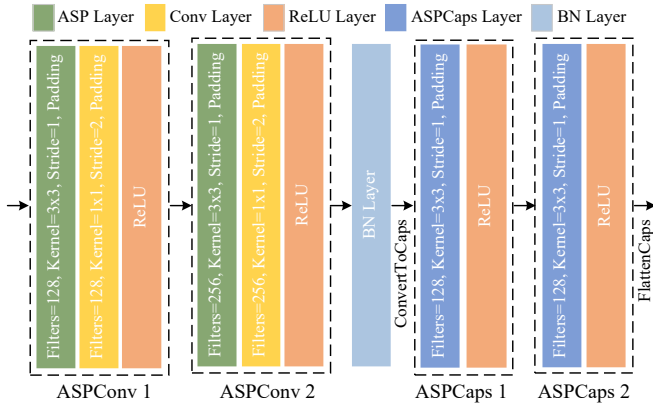


Fig. 7. Network architecture of the proposed ASPCNet model.

$$\mathbf{s}_j^{xy} = \sum_i \sum_p \sum_q \mathbf{c}_{ij}^{pq} \mathbf{u}_{j|i}^{(x+p)(y+q)}, \quad (11)$$

where \mathbf{s}_j^{xy} is the input vector of capsule j and \mathbf{c}_{ij}^{pq} denotes the coupling coefficients, which are obtained by the softmax function and updated by the dynamic routing algorithm as follows

$$\mathbf{c}_{ij}^{pq} = \frac{\exp(\mathbf{b}_{ij}^{pq})}{\sum_{j=1}^J \mathbf{b}_{ij}^{pq}}, \quad (12)$$

where J is the total number of capsules of posterior layer \mathbf{v} . \mathbf{b}_{ij}^{pq} is initialized to 0 before the training begins and is determined by the dynamic routing algorithm. In the dynamic routing algorithm, the coefficient \mathbf{b}_{ij}^{pq} is iteratively refined by measuring the agreement between the “prediction vector” $\mathbf{u}_{j|i}^{(x+p)(y+q)}$ and \mathbf{v}_j^x . If agreement is reached to a great extent, capsule $\mathbf{u}_{j|i}^{(x+p)(y+q)}$ make a good prediction for capsule \mathbf{v}_j^{xy} . Then, the coefficient \mathbf{b}_{ij}^{pq} is significantly increased. In our network, the agreement is quantified as the inner product between two vectors $\mathbf{u}_{j|i}^{(x+p)(y+q)}$ and \mathbf{v}_j^{xy} . This agreement is added to \mathbf{b}_{ij}^{pq} as follows

$$\mathbf{b}_{ij}^{pq} \leftarrow \mathbf{b}_{ij}^{pq} + \mathbf{u}_{j|i}^{(x+p)(y+q)} \cdot \mathbf{v}_j^{xy}. \quad (13)$$

Finally, the input vector is squashed by a nonlinear function (i.e., the *squash* function) to generate the output of the capsule. The detailed equations are listed below

$$\mathbf{v}_j^{xy} = \text{Squash}(\mathbf{s}_j^{xy}). \quad (14)$$

C. Architecture of the ASPCNet

In the following, we describe the whole framework of HSIC based on ASPCNet, which is shown in Fig. II-B. The whole architecture can be divided into several steps: 1) Dimension reduction by using PCA. 2) Primary feature extraction by using ASPConvs modules. 3) Hierarchical structure extraction by using ASPCaps modules. 4) Image patch-based classification. Here, the proposed ASPCNet consists of four blocks: ASPConv 1, ASPConv 2, ASPCaps 1, and ASPCaps 2, which are shown in Fig. 7. For details on the configuration of these hyper parameters, we refer the reader to the APPENDIX section.

After learning the deep ASPCNet features \mathbf{v} , we use a fully connected capsule layer to obtain digital capsule \mathbf{v}' , which is of size $T \times 16$. Then, the Euclidean norm (i.e., $\|\ell_2\|$) is used to obtain the probability vector \mathbf{v}'' for each test patch with size $T \times 1$, where each value is mapped to $[0, 1]$. Once the deep network is well-trained, for a test patch $\mathbf{Y}^{test} \in \mathbb{R}^{m \times m \times d}$, the class label of its center pixel can be determined based on the maximum probability

$$\text{Class}(\mathbf{Y}^{test}) = \arg \max_{t=1,2,\dots,T} \mathbf{v}_t''. \quad (15)$$

Here, we use the margin loss [46] as the loss function in this paper, since it can increase the probability of true classes compared with that of the traditional cross-entropy loss. For each capsule j in the last capsule layer, its loss function L_j can be calculated as follows

$$L_j = T_j \cdot \max(0, n^+ - \|\mathbf{v}_j\|)^2 + \lambda (1 - T_j) \cdot \max(0, \|\mathbf{v}_j\| - n^-)^2, \quad (16)$$

where $T_j = 1$ when class j is actually present and equals to 0 otherwise. We set $n^+ = 0.9$ and $n^- = 0.1$ as the lower bound and the upper bound for the correct class and the wrong class [46], respectively. λ is a hyper-parameter that controls the effect of gradient backpropagation in the initial phase during training. The total loss of the model is the sum of the loss of all the output capsules of the last layer.

IV. EXPERIMENTS RESULTS AND ANALYSIS

In this section, three experiments are performed on the Salinas, University of Pavia, and Houston datasets. The details of these three datasets are described as follows:

A. Datasets

- 1) *Salinas*: The first dataset is the Salinas image dataset, which was acquired by AVIRIS over the Salinas Valley in southern California. The images have 224 bands and 512×217 pixels with a spatial resolution of 3.7 m. According to the reference classification map shown in Fig. 8, there are 16 different classes labeled with different colors.
- 2) *University of Pavia*: The second dataset is called the University of Pavia dataset and was photographed by a Reflective Optics System Imaging Spectrometer (ROSIS-3) in the range of 0.46-0.86 μm over the University of Pavia. The scenes contain 115 bands and 610×340 pixels with a spatial resolution of 1.3 m per pixel. After 12 fairly noisy bands are removed, the experiments are performed using only 103 bands. Fig. 9(a-c) shows a false color composite of the University of Pavia image, the reference classification map, and the color labels, and there are 9 different classes.
- 3) *Houston*: The last image set, namely the Houston images, was captured by an ITRES-CASI 1500 sensor, and shows the University of Houston campus and its neighboring fields. The images contain 349×1905 pixels at a spatial resolution of 2.5 m per pixel and 144 bands in the range of 0.38-1.05 μm . Fig. 10 shows the false-color composite of the Indian Pines image and the corresponding reference data with 15 different classes.

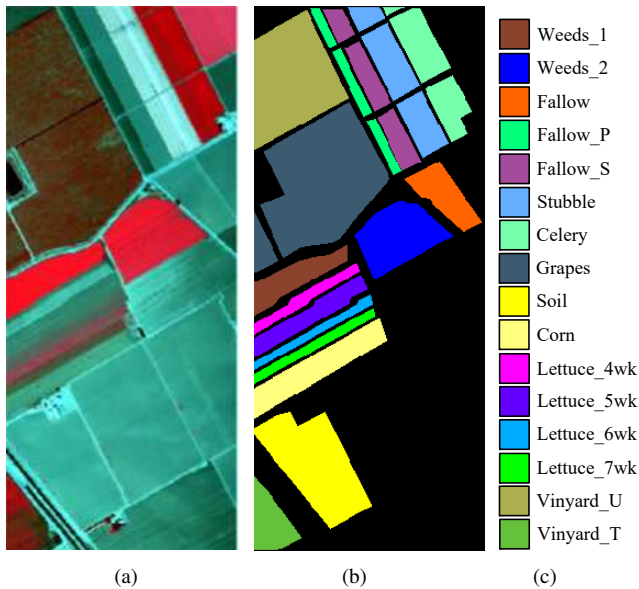


Fig. 8. The Salinas dataset. (a) Three-band color composite of the Salinas image. (b) and (c) the corresponding reference data.

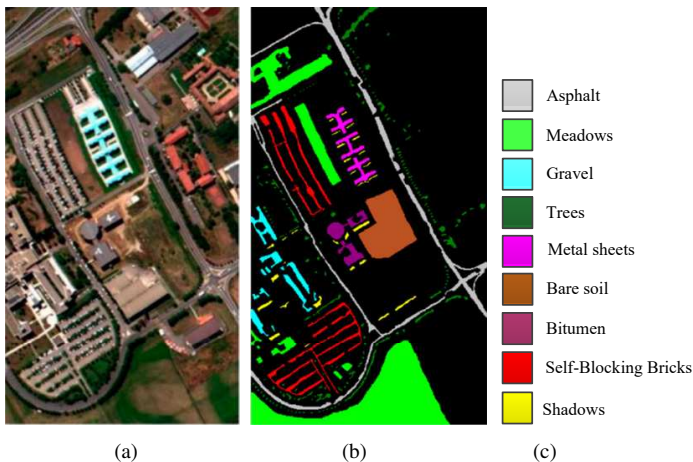


Fig. 9. The University of Pavia dataset. (a) Three-band color composite of the University of Pavia image. (b) and (c) the corresponding reference data.

B. Compared Methods

In this subsection, we compare the proposed method to other methods, i.e., a SVM [6], extreme learning machine (ELM) [62], EPF [21], deep convolution neural network (DeepCNN), CapsuleNet [47], deformable convolution neural network (DHCNet) [58], and spectral-spatial fully convolutional network (SSFCN) [42]. The implementation details of each method included in the experiments are summarized as follows.

- 1) SVM: Classification is performed with the original spectral features via an SVM classifier with an RBF kernel [6]. This algorithm is implemented using the LIBSVM library [6] and the parameters of the RBF-SVM are chosen using five-fold cross-validation.
- 2) ELM: Original spectral classification is performed with ELM [62]. This is a simple machine learning algorithm with only one hidden layer and one output layer and the

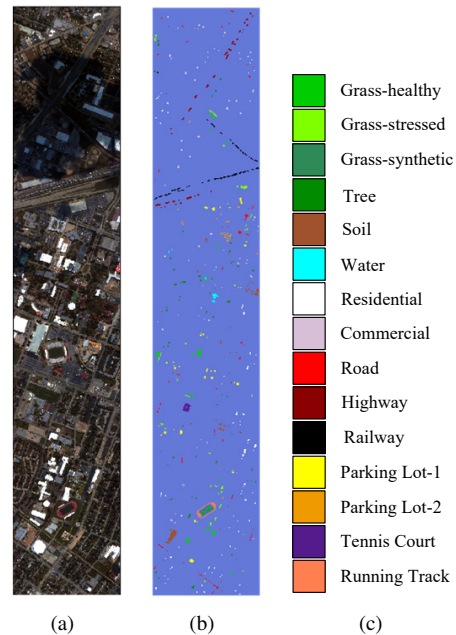


Fig. 10. The Houston dataset. (a) Three-band color composite of the Houston image. (b) and (c) the corresponding reference data.

TABLE I
THE STRUCTURE OF THE DEEPCNN METHOD. d REPRESENTS THE IMAGE DIMENSION, AND T IS THE TOTAL CLASS OF HSIS. THE STRIDE OF CONVOLUTION LAYER AND MAXPOOLING LAYER ARE SET TO 1 AND 2, RESPECTIVELY.

Layer Name	Input Shape	Kernel Size	Output Shape
Input Layer	$(27, 27, d)$	-	$(27, 27, d)$
Conv Layer	$(27, 27, d)$	$(3 \times 3 \times d, 32)$	$(27, 27, 32)$
Conv Layer	$(27, 27, 32)$	$(3 \times 3 \times 32, 32)$	$(27, 27, 32)$
Conv Layer	$(27, 27, 32)$	$(3 \times 3 \times 32, 64)$	$(27, 27, 64)$
Conv Layer	$(27, 27, 64)$	$(3 \times 3 \times 64, 64)$	$(27, 27, 64)$
Maxpooling	$(27, 27, 64)$	(2×2)	$(14, 14, 64)$
Conv Layer	$(14, 14, 64)$	$(3 \times 3 \times 64, 128)$	$(14, 14, 128)$
Conv Layer	$(14, 14, 128)$	$(3 \times 3 \times 128, 128)$	$(14, 14, 128)$
Conv Layer	$(14, 14, 128)$	$(3 \times 3 \times 128, 256)$	$(14, 14, 256)$
Conv Layer	$(14, 14, 256)$	$(3 \times 3 \times 256, 256)$	$(14, 14, 256)$
Maxpooling	$(14, 14, 256)$	(2×2)	$(7, 7, 256)$
FC Layers	(12544)	-	(1280)
FC Layers	(1280)	-	(128)
FC Layers	(128)	-	(T)

default parameters of the ELM in [62] are adopted.

- 3) EPF: This is a spectral-spatial classification method with the first 20 principal components determined via guided filter-based EPF. We use the default parameters of a filtering size r and blur degree ε to 3 and 0.2, respectively [21], in the implementations.
- 4) DeepCNN: Spatial classification is performed via a 3D-CNN method with the first 20 principal components. The architecture is shown in Table I. For each pixel, a patch size of 27×27 is extracted as the input of the network. This algorithm is trained using the Adam optimizer with a learning rate of $5e-4$.
- 5) CapsuleNet: The original capsule network-based HSIC method with the original spectral information [47]. The architecture adopts the Adam optimizer with a learning rate equal to 0.001, 100 training epochs, and a patch size of 15×15 .

TABLE II

THE STRUCTURE OF THE PROPOSED ASPCNET METHOD. d REPRESENTS IMAGE DIMENSION, AND T IS THE TOTAL CLASS OF HSI. THE STRIDE OF CONVOLUTION LAYERS ARE DESCRIBED IN APPENDICES A.

Layer Name	Input Shape	Kernel Size	Output Shape
Input Layer	$(27, 27, d)$	-	$(27, 27, d)$
ASP Layer 1	$(27, 27, d)$	$(3 \times 3 \times d, 128)$	$(27, 27, 128)$
Conv Layer	$(27, 27, 128)$	$(1 \times 1 \times 128, 128)$	$(14, 14, 128)$
ASP Layer 2	$(14, 14, 128)$	$(3 \times 3 \times 128, 256)$	$(14, 14, 256)$
Conv Layer	$(14, 14, 256)$	$(1 \times 1 \times 256, 256)$	$(7, 7, 256)$
BN Layer	$(7, 7, 256)$	-	$(7, 7, 256)$
ConvertToCaps	$(7, 7, 256)$	-	$(7, 7, 256, 1)$
ASPCaps Layer 1	$(7, 7, 256, 1)$	$(3 \times 3 \times 256, 32, 4)$	$(7, 7, 32, 4)$
ASPCaps Layer 2	$(7, 7, 32, 4)$	$(3 \times 3 \times 128, 32, 4)$	$(7, 7, 32, 4)$
FlattenCaps	$(7, 7, 32, 4)$	-	$(1568, 4)$
DigitalCaps	$(1568, 4)$	$(T, 1568, 16, 4)$	$(T, 16)$
CapsToScalars	$(T, 16)$	-	$(T, 1)$

TABLE III

NUMBERS OF TRAINING AND TESTING SAMPLES IN SALINAS DATASET.

Class Name	Total	Training	Testing
Brocoli green weeds 1	2009	40	1969
Brocoli green weeds 2	3726	76	3650
Fallow	1976	38	1938
Fallow rough plow	1394	26	1368
Fallow smooth	2678	52	2626
Stubble	3959	79	3880
Celery	3579	70	3509
Grapes untrained	11271	225	11046
Soil vinyard develop	6203	124	6079
Corn senesced weeds	3278	21	3257
Lettuce romaine 4wk	1068	21	1047
Lettuce romaine 5wk	1927	38	1889
Lettuce romaine 6wk	916	18	898
Lettuce romaine 7wk	1070	20	1050
Vinyard untrained	7268	140	7128
Vinyard treils	1807	36	1771
Total	54129	1024	53105

- 6) DHCNet: This is a deformable convolution neural network for HSIC with the first 3 principal components. According to the implementations [58], the patch size, the momentum of the batch normalization layer, and the training epoch are set to 29×29 , 0.9, and 1500, respectively.
- 7) SSFCN: This is a spectral-spatial FCN with conditional random fields. The detailed architecture and default parameters of the network follow the implementations in [42]. The network is trained with a learning rate of $5e-4$ using the Adam optimizer.
- 8) ASPCNet: This is the proposed spectral-spatial ASPC neural network. The detailed architecture of the network is shown in Table II. We set the batch size and training epoch to 96 and 200, respectively. The momentum of the batch normalization layer is set to 0.9. The network is trained using the Adam optimizer with a learning rate of $5e-4$, beta_1 of 0.9, beta_2 of 0.999, and epsilon of $1e-8$.

All of the methods are carried out on a desktop computer with a Windows 10 OS, an Intel i9-10900F 2.8-GHz processor with 64 GB of RAM, and a single NVIDIA GTX2080Ti GPU. DeepCNN, CapsuleNet, DHCNet, SSFCN, and ASPCNet are constructed by using the Keras framework, CUDA 10, and Python 3.6.5 as the programming language. The SVM, ELM, and EPF methods are carried out in MATLAB R2020a without GPU acceleration.

TABLE IV

NUMBERS OF TRAINING AND TESTING SAMPLES IN UNIVERSITY OF PAVIA DATASET.

Class Name	Total	Training	Testing
Asphalt	6631	200	6431
Meadows	18649	200	18449
Gravel	2099	200	1899
Trees	3064	200	2864
Metal sheets	1345	200	1145
Bare soil	5029	200	4829
Bitumen	1330	200	1130
Self-Blocking Bricks	3682	200	3482
Shadows	947	200	747
Total	42776	1800	40976

TABLE V

NUMBERS OF TRAINING AND TESTING SAMPLES IN HOUSTON DATASET.

Class Name	Total	Training	Testing
Grass-healthy	1251	160	1091
Grass-stressed	1254	160	1094
Grass-synthetic	697	80	617
Tree	1244	160	1084
Soil	1242	160	1082
Water	325	80	245
Residential	1268	160	1108
Commercial	1244	160	1084
Road	1252	160	1092
Highway	1227	160	1067
Railway	1235	160	1075
Parking Lot-1	1233	160	1073
Parking Lot-2	469	80	389
Tennis Court	428	80	348
Running Track	660	80	580
Total	15029	2000	13029

C. Quantitative Metrics

To effectively evaluate the classification performance of different methods, three objective indexes, i.e., the overall accuracy (OA), average accuracy (AA), and Kappa coefficient (Kappa) are adopted in the experiments. Specifically, the OA value represents the percentage of all test pixels that are correctly classified. the AA value measures the mean of all class accuracies. Taking the uncertainty factors of the classification into consideration, the Kappa value is proposed, which represents the percentage of correctly classified pixels corrected by the degree of agreement.

D. Analysis of the influences of different parameters

In this subsection, a detailed analysis of the influence of three parameters (i.e., the number of dimensions d , patch size $m \times m$ and dilation rate h_{dr}) on the image classification performance is conducted on three real datasets.

1) *Analysis of the influence of the number of dimensions:* first, we analyze the influence of the number of dimensions (the principal components) of HSI under different settings. Fig. 11 shows the influence of parameter d on three different datasets, i.e., the Salinas, University of Pavia, and Houston datasets. As seen in Fig. 11(a), for the Salinas dataset, the classification performance of the ASPCNet method increases first and then decreases slightly when $d > 15$ as parameter d increases because the first several components include most of the spatial information. With an increasing number

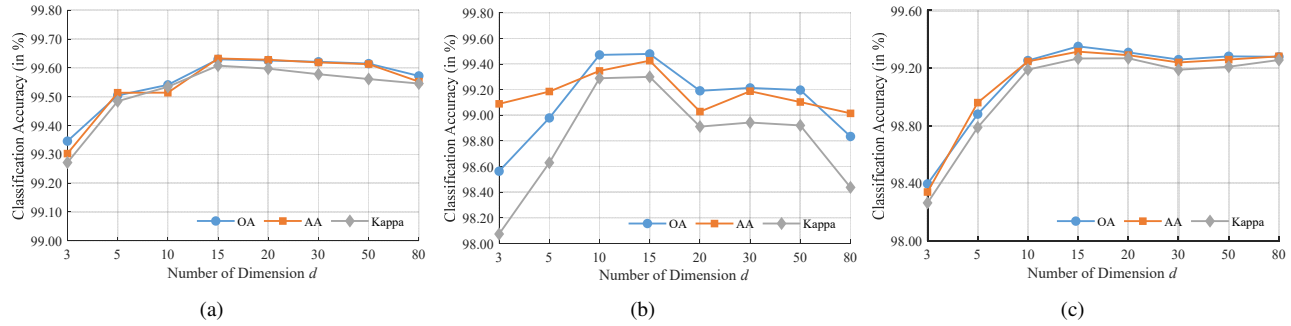


Fig. 11. The effects of the number of dimension d based on the proposed method for three real datasets: (a) Salinas, (b) University of Pavia, (c) Houston.

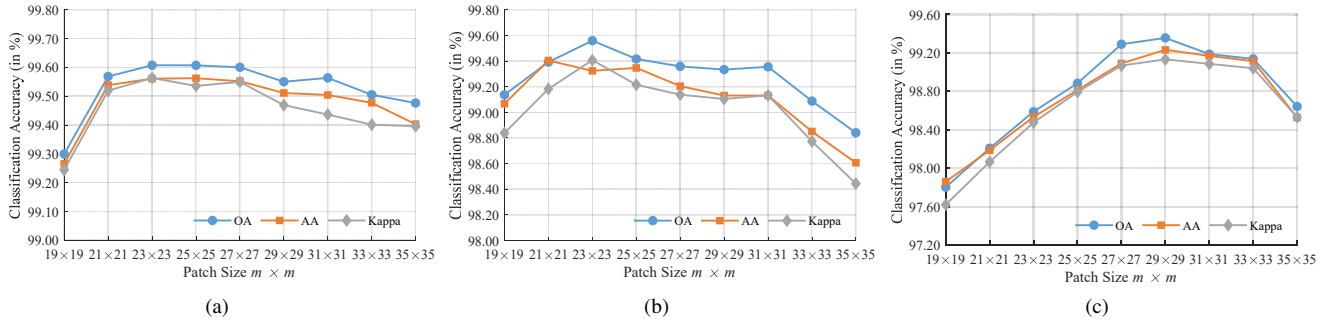


Fig. 12. The effects of the patch size $m \times m$ based on the proposed method for three real datasets: (a) Salinas, (b) University of Pavia, (c) Houston.

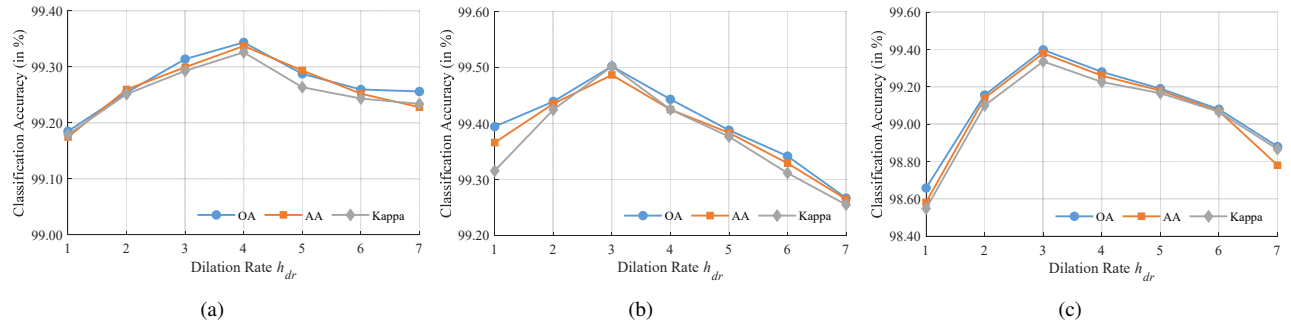


Fig. 13. The effects of the dilation rate h_{dr} based on the proposed method for three real datasets: (a) Salinas, (b) University of Pavia, (c) Houston.

of components, there is much extra even noisy information among the HSI bands, and this situation is even worse for a complex dataset such as the University of Pavia (see Fig. 11(b)). In addition, a similar phenomenon can be seen on the Houston datasets in Fig. 11(c). Therefore, $d = 15$ is set as the default parameter among all datasets.

2) *Analysis of the influence of the patch size*: second, we discuss the influence of the patch size m of OA under different settings. Experiments are conducted on the three datasets. For instance, Fig. 12(a) denotes different patch sizes on the Salinas dataset, showing the OA values versus different settings of patch size m varying from 19×19 to 35×35 with an interval of 2. As seen, as the parameter m increases, the OA increases first and declines later. Experimental results indicate that it can extract more local spatial features at first. As m increases (e.g., 35×35), it may introduce extra information as interference. The same conclusion is reached for the other two datasets. Therefore, in consideration of the trade-off between

classification performance and the number of parameters, a patch size of 27×27 is adopted as the default parameter.

3) *Analysis of the influence of the dilation rate*: the third experiment is conducted on the three datasets to evaluate the classification performance under different dilation rate settings. In general, a CNN uses a pooling operation to increase the receptive field. Unfortunately, some materials may "disappear" after several pooling layers. Dilated convolutions can avoid this problem in an elegant way, in which the dilation rate h_{dr} exerts control. Here, Fig. 13 shows the influence of the dilation rate h_{dr} on the three different datasets. As we can see from Fig. 13(a), as the dilation rate h_{dr} increases, OA increases first when $h_{dr} < 4$ and then decreases when $h_{dr} > 4$ on the Salinas dataset. For the University of Pavia and Houston datasets, shown in Fig. 13(b) and (c), the proposed ASPCNet can obtain the highest accuracies when h_{dr} equals 3. Therefore, for the Salinas, University of Pavia and Houston datasets, the default parameters are set as $h_{dr} = 4$, $h_{dr} = 3$, and $h_{dr} = 3$,

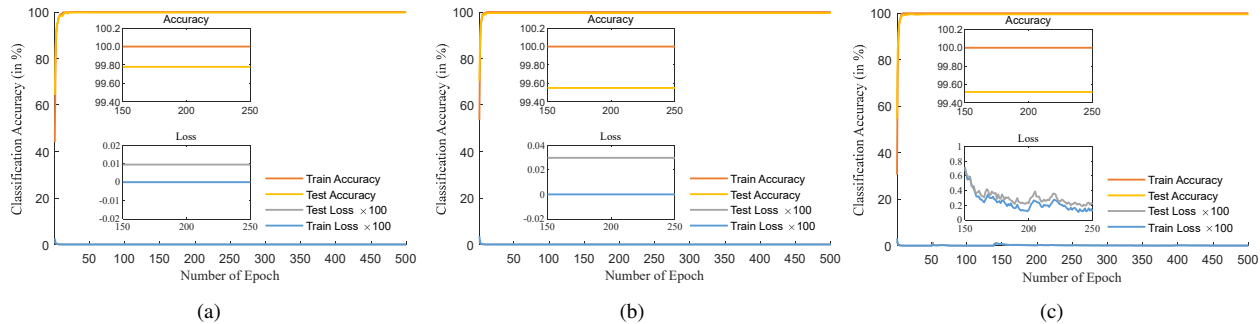


Fig. 14. The effects of the training epoch based on the proposed method for three real datasets. (a) Salinas, (b) University of Pavia, (c) Houston.

TABLE VI
CLASSIFICATION ACCURACIES (%) ON SALINAS DATASET AMONG DIFFERENT METHODS. NUMBER IN PARENTHESIS INDICATES THE STANDARD VARIANCE OF THE REPEATED EXPERIMENTS. THE BEST AND SECOND BEST RESULTS ARE SHOWN IN RED AND BLUE COLORS, RESPECTIVELY.

Classes	SVM	ELM	EPF	DeepCNN	CapsuleNet	DHCNet	SSFCN	ASPCNet
1	99.94(0.08)	99.95(0.10)	100.00(0.0)	99.08(0.95)	99.90(1.35)	95.99(2.89)	99.81(0.39)	99.96(0.06)
2	99.07(0.41)	99.24(0.34)	99.94(0.12)	99.69(0.61)	99.95(0.46)	98.76(0.89)	100.00(0.0)	99.99(0.01)
3	93.54(1.02)	97.16(0.33)	95.99(0.77)	99.87(0.12)	99.48(0.27)	99.55(0.41)	100.00(0.0)	100.00(0.0)
4	97.36(1.19)	99.13(0.53)	98.17(0.38)	95.54(4.69)	98.10(0.60)	98.51(1.59)	99.53(0.51)	98.51(1.11)
5	98.29(0.71)	98.58(0.48)	99.91(0.06)	98.83(1.34)	99.89(1.04)	99.86(0.17)	99.22(0.55)	99.08(0.93)
6	99.91(0.13)	99.98(0.01)	99.98(0.02)	99.12(1.14)	99.82(0.27)	99.59(0.75)	100.00(0.0)	99.98(0.18)
7	99.16(0.75)	99.73(0.13)	99.91(0.12)	99.77(0.36)	99.00(0.64)	99.56(0.52)	99.86(0.07)	100.00(0.0)
8	76.53(1.39)	79.72(0.77)	80.67(2.04)	99.27(0.55)	99.77(1.07)	98.86(0.93)	98.23(0.82)	99.89(0.19)
9	99.02(0.23)	98.70(0.24)	99.33(0.03)	100.00(0.0)	99.11(0.33)	99.94(0.11)	100.00(0.0)	100.00(0.0)
10	94.42(1.56)	98.56(0.52)	98.20(1.03)	83.32(10.8)	87.50(2.30)	97.45(3.63)	97.65(1.66)	99.06(0.34)
11	90.66(3.72)	93.96(1.35)	96.73(1.45)	94.96(3.25)	98.57(3.48)	99.58(0.36)	99.92(0.15)	99.68(0.32)
12	95.30(0.78)	94.94(0.75)	99.09(0.33)	97.49(2.68)	99.41(0.65)	99.93(0.09)	99.98(0.03)	99.89(0.18)
13	95.91(1.27)	94.33(3.13)	98.73(1.37)	97.57(2.84)	97.66(1.08)	99.60(0.55)	99.91(0.08)	97.43(2.97)
14	95.33(0.80)	96.94(1.63)	98.63(0.88)	97.77(1.03)	98.38(1.66)	99.73(0.30)	99.20(0.53)	99.43(0.82)
15	74.65(2.73)	79.07(1.30)	89.73(2.26)	99.78(0.21)	97.95(0.97)	99.56(0.30)	98.38(0.47)	99.10(1.08)
16	98.31(0.38)	99.61(0.18)	99.98(0.04)	99.77(0.32)	97.63(1.35)	98.05(1.31)	99.63(0.20)	100.00(0.0)
OA	90.04(0.67)	91.96(0.15)	93.71(0.69)	98.20(0.57)	98.48(0.47)	99.10(0.17)	99.17(0.14)	99.68(0.16)
AA	94.21(0.51)	95.60(0.19)	97.25(0.27)	97.61(0.58)	98.30(0.36)	99.03(0.22)	99.36(0.09)	99.50(0.21)
Kappa	88.89(0.75)	91.02(0.17)	92.98(0.77)	98.00(0.63)	98.31(0.52)	99.00(0.19)	99.08(0.15)	99.53(0.18)

respectively.

Finally, we analyze the impact of the training epoch on the accuracies and losses of training and testing. From Fig. 14, it can be found that the proposed ASPCNet method can quickly converge with little oscillation. For example, it can always reach the maximum training accuracies when the epoch $\in [25, 30]$. Therefore, if we want to improve the training efficiency in practical engineering applications, we can use the “*early-stopping*” operation; that is, when the training accuracies reach the local maximum and there are no better training accuracies in the subsequent training epochs, the training processing is automatically stopped.

E. Classification Results

In this section, the proposed method named ASPCNet is compared with different well-known classification methods, including traditional machine learning-based methods such as SVM [6], ELM [62], and EPF [21] and state-of-the-art (SOTA) deep learning-based methods such as DeepCNN, CapsuleNet [47], DHCNet [58], and SSFCN [42], on the Salinas, University of Pavia and Houston datasets. To evaluate the aforementioned three quantitative metrics, i.e., OA, AA and the Kappa, each experiment is repeated approximately 20 times for each classification method.

The first experiment is conducted on the Salinas dataset. Here, 2% of the labeled image patches are randomly chosen as the training patches to train the parameters of the network and the rest of the patches are viewed as test patches, as seen in Table III. The classification performance and the corresponding classification maps obtained by the nine methods are exhibited in Table VI and Fig. 15. The numbers in parentheses indicate the standard variances, and the best and second best results are highlighted in red and blue, respectively. The SVM classifier obtains the worst classification accuracy on the Salinas dataset, which indicates that only using spectral information is not enough for complex HSIs. By taking the spatial information of HSI into consideration, traditional machine learning-based methods such as EPF can achieve better results with 93.71%. Furthermore, image patch-based classifiers such as DeepCNN and CapsuleNet, which both obtain greater than 98% classification accuracies, indicate that image patch-based classifiers truly play an important role in HSIC. As seen from Fig. 15(e)-(f), there are some misclassified samples in the CapsuleNet and DHCNet results, especially for the grapes untrained class, the Broccoli green weeds 2 class, and the Vinyard untrained class, which demonstrates that there is still improvement space. Moreover, the SSFCN is a more efficient method that can avoid patch extraction and was a new SOTA in 2020. By contrast,

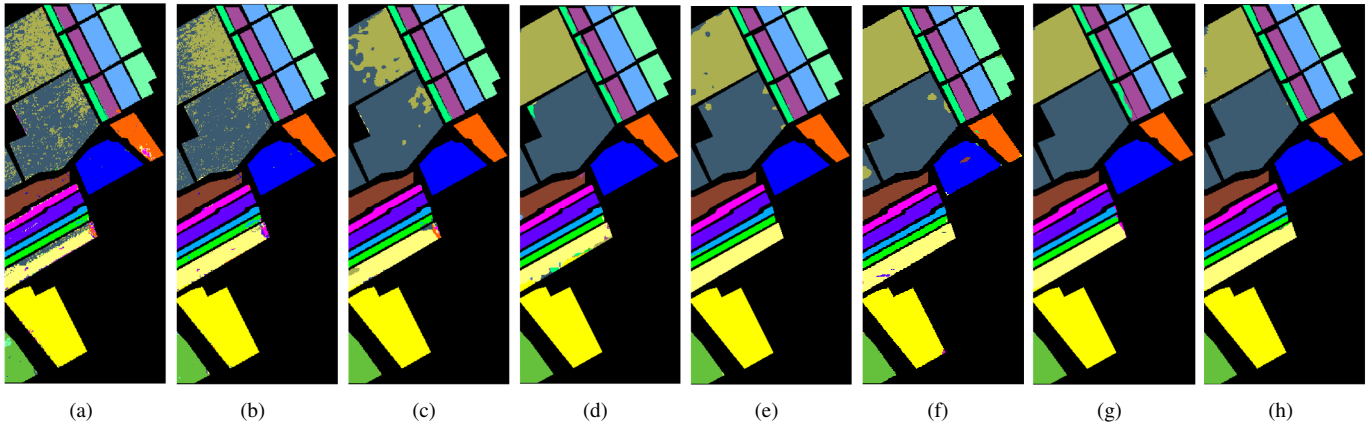


Fig. 15. Classification maps obtained by nine methods on the Salinas dataset: (a) SVM (90.04%), (b) ELM (91.96%), (c) EPF (93.71%), (d) DeepCNN (98.20%), (e) CapsuleNet (98.48%), (f) DHCNet (99.10%), (g) SSFCN (99.17%), and (h) ASPCNet (99.68%).

TABLE VII

CLASSIFICATION ACCURACIES (%) ON UNIVERSITY OF PAVIA DATASET AMONG DIFFERENT METHODS. NUMBER IN PARENTHESIS INDICATES THE STANDARD VARIANCE OF THE REPEATED EXPERIMENTS. THE BEST AND SECOND RESULTS ARE SHOWN IN RED AND BLUE COLORS, RESPECTIVELY.

Classes	SVM	ELM	EPF	DeepCNN	CapsuleNet	DHCNet	SSFCN	ASPCNet
CA	1	97.15(0.22)	97.46(0.44)	98.46(0.32)	97.16(2.00)	97.20(1.21)	98.66(0.73)	98.54(0.99)
	2	97.67(0.29)	96.96(0.28)	99.52(0.15)	98.87(0.47)	98.91(0.77)	99.09(0.25)	99.75(0.32)
	3	77.89(1.35)	69.34(1.55)	96.16(2.07)	99.25(1.31)	98.05(0.83)	99.49(0.69)	99.84(0.18)
	4	87.88(3.28)	91.14(0.54)	98.79(1.46)	92.86(3.75)	98.87(0.43)	99.28(0.29)	97.81(0.70)
	5	97.61(0.97)	99.41(0.19)	99.53(0.60)	99.55(0.49)	99.74(0.20)	99.88(0.17)	99.23(0.20)
	6	79.82(3.44)	77.44(1.31)	95.59(2.04)	99.79(0.40)	99.66(0.26)	99.97(0.03)	99.69(0.04)
	7	66.69(3.64)	63.11(2.04)	92.97(8.57)	99.98(0.04)	98.55(0.57)	99.98(0.04)	99.77(0.08)
	8	86.76(0.87)	81.31(1.17)	93.60(0.64)	97.85(0.82)	98.64(0.40)	99.59(0.24)	98.03(0.72)
	9	99.84(0.10)	99.97(0.05)	98.95(0.95)	98.15(0.91)	100.00(0.0)	98.90(0.49)	99.23(0.72)
OA	88.24(0.72)	89.70(0.37)	97.91(0.39)	98.26(0.46)	98.70(0.56)	99.25(0.16)	99.28(0.24)	99.58(0.13)
AA	87.92(0.79)	86.24(0.37)	97.06(0.95)	98.16(0.61)	98.85(0.35)	99.23(0.10)	99.14(0.25)	99.55(0.09)
Kappa	88.37(0.91)	86.34(0.48)	97.19(0.53)	97.66(0.61)	98.25(0.75)	98.99(0.21)	99.23(0.33)	99.44(0.13)

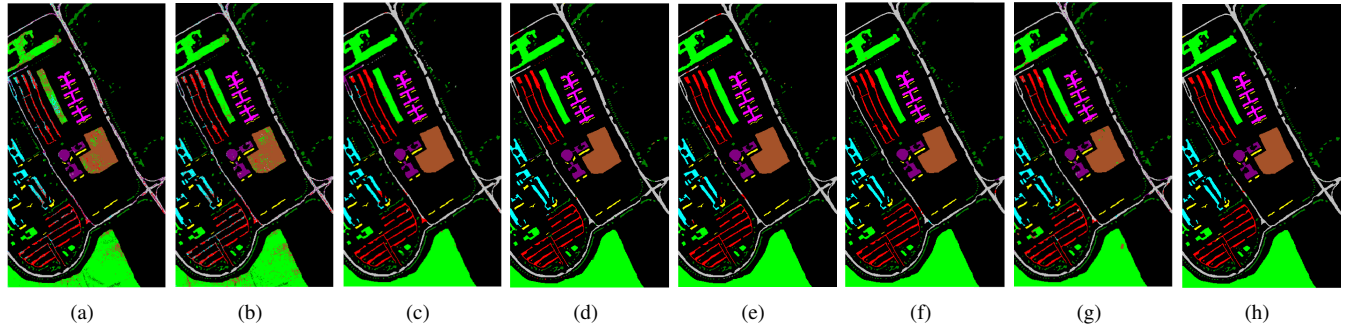


Fig. 16. Classification maps obtained by nine methods on the University of Pavia dataset: (a) SVM (88.24%), (b) ELM (89.70%), (c) EPF (97.91%), (d) DeepCNN (98.26%), (e) CapsuleNet (98.70%), (f) DHCNet (99.25%), (g) SSFCN (99.28%), and (h) ASPCNet (99.58%).

the proposed ASPCNet uses a new framework by developing the adaptive spatial unit into the original capsulenet, which can better adapt to the complex spatial characteristics of the HSI. In addition, ASPCNet can obtain the highest classification accuracies in terms of OA, AA, and Kappa with a smaller variance.

The second experiment is performed on the University of Pavia dataset. First, 200 samples per class are selected randomly as the training samples and the rest are used as test samples (see Table IV). Table VII shows the classification performance of the different methods, and Fig. 16 displays the corresponding classification maps. As seen, there are three

classes that can be classified 100% correctly by the proposed ASPCNet, and ASPCNet achieves the highest accuracies on seven classes, which shows the outstanding performance of ASPCNet. Moreover, as we can see from Fig. 16, ASPCNet provides more homogeneous classification maps with clear object edges, even for the University of Pavia dataset, with complex structures.

Then, similar conclusions can be observed on the Houston dataset, for which training samples are shown in Table V and the classification results and maps are displayed in Table VIII and Fig. 17, respectively. The classification results of ASPCNet are consistently better than those of the compared

TABLE VIII
CLASSIFICATION ACCURACIES (%) ON HOUSTON DATASET AMONG DIFFERENT METHODS. NUMBER IN PARENTHESIS INDICATES THE STANDARD VARIANCE OF THE REPEATED EXPERIMENTS. THE BEST AND SECOND RESULTS ARE SHOWN IN RED AND BLUE COLORS, RESPECTIVELY.

Classes	SVM	ELM	EPF	DeepCNN	CapsuleNet	DHCNet	SSFCN	ASPCNet
1	96.15(0.69)	97.70(1.03)	98.15(1.10)	97.92(0.75)	98.11(1.39)	99.62(0.23)	99.82(0.18)	100.00(0.0)
2	97.81(0.27)	98.25(0.75)	98.30(0.67)	98.27(0.77)	98.32(1.51)	99.69(0.20)	99.63(0.18)	99.95(0.05)
3	99.65(0.60)	100.00(0.0)	100.00(0.0)	100.00(0.0)	97.86(1.14)	99.50(0.52)	99.11(0.57)	99.53(1.31)
4	98.47(0.80)	99.07(0.65)	98.83(0.96)	99.55(0.23)	95.02(2.10)	97.64(2.07)	99.16(0.65)	99.26(0.65)
5	96.33(1.38)	98.09(0.78)	97.64(2.09)	97.29(1.38)	99.82(0.37)	99.41(0.11)	100.00(0.0)	99.45(0.55)
6	99.25(0.60)	100.00(0.0)	100.00(0.0)	100.00(0.0)	96.98(2.70)	99.26(0.49)	99.37(0.61)	99.38(0.21)
7	91.58(1.91)	93.75(1.53)	93.97(2.56)	94.70(1.12)	97.24(1.61)	98.57(1.13)	98.47(1.35)	99.55(0.27)
8	89.26(3.30)	96.15(0.39)	97.67(1.65)	96.41(0.28)	97.90(0.57)	96.07(1.58)	95.20(1.85)	98.84(0.24)
9	88.32(2.19)	87.75(2.22)	96.18(1.94)	91.46(6.08)	95.70(2.54)	99.45(0.43)	99.45(0.55)	99.45(0.46)
10	92.07(1.80)	86.60(1.58)	97.02(1.35)	92.19(4.95)	100.00(0.0)	99.24(0.70)	100.00(0.0)	100.00(0.0)
11	88.04(1.47)	89.26(0.75)	95.05(1.24)	92.19(2.48)	100.00(0.0)	99.16(0.83)	99.49(0.51)	100.00(0.0)
12	88.00(1.62)	87.98(1.89)	88.48(3.13)	89.93(2.10)	99.74(0.15)	99.26(0.20)	99.77(0.23)	98.27(1.35)
13	74.25(6.36)	90.47(3.55)	80.96(4.37)	87.01(3.26)	100.00(0.0)	98.87(0.82)	98.71(0.51)	97.04(2.44)
14	96.56(0.43)	95.72(1.80)	99.03(1.37)	96.83(2.60)	100.00(0.0)	99.74(0.99)	100.00(0.0)	100.00(0.0)
15	99.09(0.62)	99.86(0.20)	100.00(0.0)	99.96(0.08)	99.07(0.78)	99.53(0.14)	100.00(0.0)	100.00(0.0)
OA	93.01(0.54)	94.08(0.19)	96.22(0.33)	95.35(1.09)	98.28(0.45)	99.02(0.23)	99.16(0.12)	99.39(0.03)
AA	92.99(0.71)	94.71(0.28)	96.09(0.41)	95.58(0.79)	98.38(0.47)	99.01(0.20)	99.22(0.03)	99.31(0.08)
Kappa	92.43(0.59)	93.60(0.21)	95.91(0.35)	94.97(1.18)	98.14(0.49)	99.04(0.24)	99.10(0.13)	99.34(0.03)

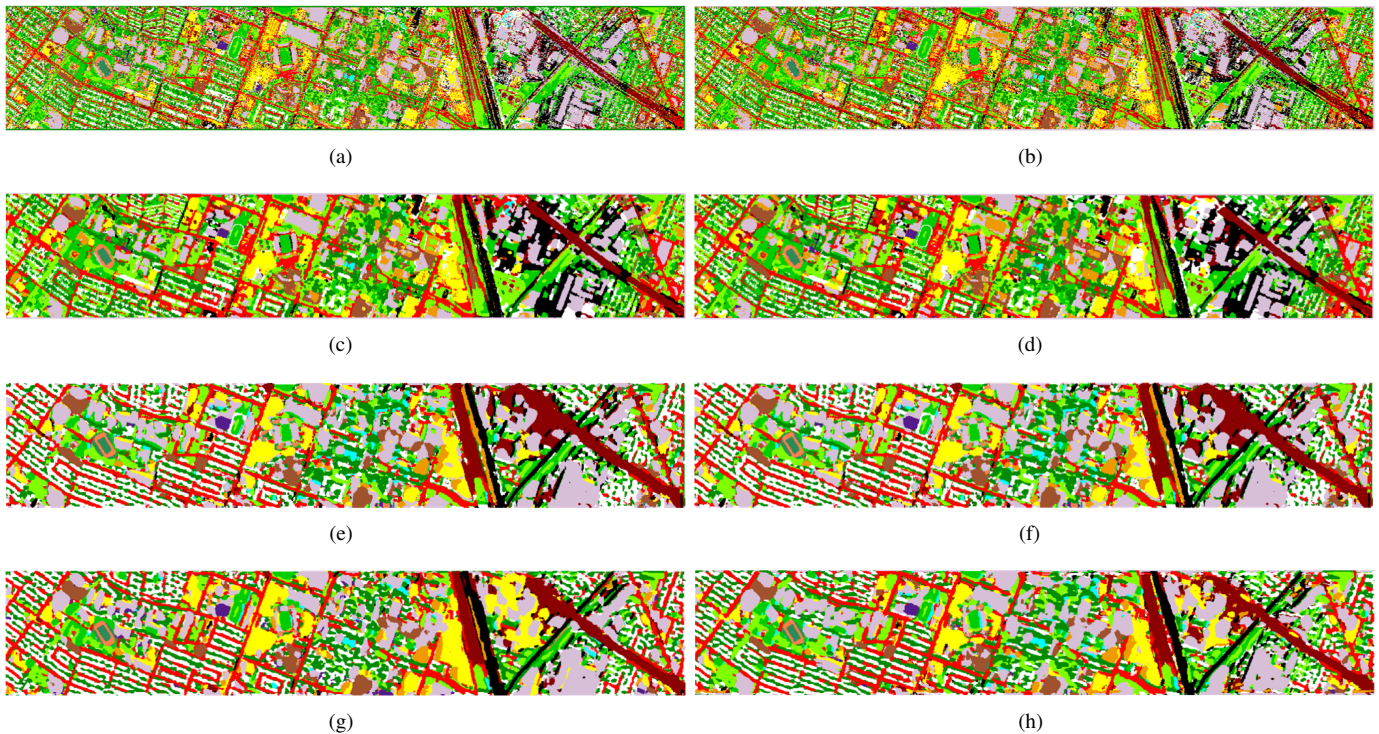


Fig. 17. Classification maps obtained by nine methods on the Houston dataset: (a) SVM (93.01%), (b) ELM (94.08%), (c) EPF (96.22%), (d) DeepCNN (95.35%), (e) CapsuleNet (98.28%), (f) DHCNet (99.02%), (g) SSFCN (99.16%), and (h) ASPCNet (99.39%).

spectral-spatial classification methods, and the experimental results from the three real datasets indicate the robustness of the proposed ASPCNet method.

Last, experiments conducted on three datasets indicate the effectiveness of the proposed method with a small number of training samples. Here, the number of the training samples is 40 for each class, which is selected randomly. Table IX shows the OA, AA, and kappa obtained by different methods of three datasets. As seen from Table IX, whatever compared with traditional machine learning-based methods or deep learning-based methods, the proposed ASPCNet method can always obtain a better result. More importantly, the proposed method

shows obvious improvements in terms of OA, AA, and kappa with a smaller variance.

F. Comparison of Different Feature Fusion Steps

To measure the performance of different components of the proposed ASPCNet, an experiment is performed on the University of Pavia dataset with 40 training samples per class. The experimental results are shown in Table X. As seen, Dil, Def, and Dil-Def refer to learning the primary convolution feature using the dilated convolution, deformable convolution, and Dil-Def convolution, respectively. Note that Dil-Def and ASPCConv are different. The Dil-Def convolution means that the

TABLE IX

CLASSIFICATION ACCURACIES (%) OF DIFFERENT METHODS ON THREE DATASETS WITH 40 TRAINING SAMPLES PER CLASS. NUMBER IN PARENTHESIS INDICATES THE STANDARD VARIANCE OF THE REPEATED EXPERIMENTS. THE BEST AND SECOND RESULTS ARE SHOWN IN RED AND BLUE COLORS, RESPECTIVELY.

Datasets	Index	SVM	ELM	EPF	DeepCNN	CapsuleNet	DHCNet	SSFCN	ASPCNet
Salinas	OA	85.86(1.29)	89.89(0.45)	91.25(2.33)	92.24(4.39)	93.00(2.54)	94.09(0.72)	94.64(2.26)	96.97(2.13)
	AA	90.68(0.40)	93.59(0.21)	94.72(0.60)	94.29(2.15)	95.61(1.40)	96.26(0.28)	96.55(1.12)	97.73(0.65)
	Kappa	84.31(1.42)	88.74(0.50)	90.28(2.56)	91.31(4.96)	92.18(2.85)	93.42(0.81)	94.02(2.52)	96.81(2.35)
University of Pavia	OA	82.14(1.39)	84.50(0.57)	92.88(2.72)	92.67(2.85)	93.22(1.97)	95.29(1.91)	96.73(0.91)	97.84(0.65)
	AA	79.99(0.99)	81.50(0.78)	92.39(2.18)	92.36(1.79)	92.42(1.58)	95.30(1.25)	96.66(0.67)	97.40(0.52)
	Kappa	77.09(1.67)	79.83(0.66)	90.73(3.48)	90.39(3.67)	91.07(2.53)	95.23(2.49)	94.86(1.20)	97.13(0.86)
Houston	OA	87.47(0.72)	88.71(0.50)	91.79(1.10)	88.98(1.47)	92.96(1.50)	93.57(0.54)	94.38(0.58)	95.42(0.57)
	AA	87.27(1.30)	89.54(0.46)	91.34(1.69)	90.90(1.10)	94.11(1.31)	94.60(0.63)	95.27(0.44)	96.03(0.55)
	Kappa	86.45(0.77)	87.79(0.53)	91.12(1.19)	88.08(1.59)	92.39(1.62)	93.04(0.59)	93.93(0.62)	95.04(0.61)

TABLE X

CLASSIFICATION ACCURACIES (%) OF DIFFERENT STEPS OF THE ASPCNET ON THE UNIVERSITY OF PAVIA DATASET WITH 40 TRAINING SAMPLES PER CLASS.

Indexes	ASPCaps-based			ASPConvs-based		ASPCNet
	Dil	Def	Dil-Def	Caps	ConvCaps	
OA	91.35	92.88	93.58	94.31	94.99	97.81
AA	88.78	92.33	93.28	95.13	95.45	98.14
Kappa	88.62	90.62	91.53	94.32	95.42	97.13

network conducts dilated convolution first and then deformable convolution later (two layers totally), whereas ASPConv aims to integrate the dilation and deformation operations into one unit (only a single layer). Caps and ConvCaps refer to learning digitalCaps features using the original capsule network and conv-capsule network with digital feature extraction.

In the proposed ASPCNet method, we create an ASP unit by taking advantage of both dilated and deformable convolution operations, which can simultaneously expand the receptive field and rotate the sampling location, and effectively avoid grid effects. Note that we develop the ASP unit into a traditional capsulenet during the primarycaps and digitalcaps process. Based on the experimental results observations, the Dil, Def, and Dil-Def operations lead to lower OAs of 91.35%, 92.88%, and 93.58%, respectively. Especially, the classification performance obtained by ASPCNet is better than that of Dil-Def, which indicates that the ASP unit is not a simple combination of the Dil and Def operations, like stacking one to another. By contrast, the ASP unit combines the Dil and Def operations into a unit, improving the classification performance by adaptively enlarging the receptive field and adapting the shapes according to the complex features of HSIs. Based on the ASPConvs modules, we compare the output classifier using traditional caps, ConvCaps, and ASPCaps. According to the experimental results, we find that the proposed ASPCNet can obtain the highest result of the three methods, approximately 97.81% (traditional caps and ConvCaps can only obtain 94.31% and 94.99%, respectively). The results demonstrate that the ASPCaps located in the Caps layer can help improve classification performance.

G. Computing Times of Different Methods

The time consumption (in seconds) of the training processes of the proposed ASPCNet and the other compared methods

TABLE XI

COMPUTATIONAL TIME (IN SECONDS) OF DIFFERENT METHODS, AND TRAINING SAMPLES ARE SHOWN IN TABLE III, IV AND V.

Methods	Datasets		
	Salinas	University of Pavia	Houston
SVM	120.81	109.81	230.46
ELM	4.2	3.34	6.15
EPF	123.55	107.13	238.55
DeepCNN	133.51	210.18	323.98
CapsuleNet	158.54	237.89	381.25
DHCNet	215.52	261.34	270.69
SSFCN	350.41	389.45	623.5
ASPCNet	183.61	241.92	313.81

on the three typical hyperspectral datasets are reported in Table XI. The experimental environments are described at the end of Section IV-B. The traditional machine learning methods (SVM, ELM, and EPF) and some related deep learning methods (DeepCNN, CapsuleNet, DHCNet, and SSFCN) are compared with the proposed ASPCNet. As observed, the proposed ASPCNet method requires more computational time than all the traditional machine learning methods, and the proposed method's main computational cost is due to the dynamic routing algorithm in capsulenet. When compared with DHCNet and SSFCN, the ASPCNet method needs less time on the same benchmark. To make the network more efficient and better able to be transformed for other application fields, searching for a lightweight neural network will be a focus of our future research.

V. CONCLUSIONS

In this paper, we develop an adaptive spatial pattern capsule network (ASPCNet) for image classification, in which a unique convolutional unit called the ASP unit is used to extract features. On the research basis of the conv-capsulenet, the ASP units are introduced twice into the capsulenet during the classification process. Initially, instead of using a shallow convolutional layer, the proposed ASPCNet uses ASPConvs to extract the relatively high-level features before they are fed into primarycaps, making it easier to transfer hierarchical relationships between low-level and high-level capsules. Furthermore, considering the fixed sampling location of the convolutional kernels, ASPCaps is further introduced to this model, making full use of contextual information adaptively and meeting the requirements of HSIC tasks of complex

structures. In addition, the experimental results on three real HSIs demonstrate the superiority of the proposed ASPCNet over several compared methods in terms of the visual qualities of the classification map and quantitative metrics.

APPENDIX A

PROOF OF THE SECTION III-C PART

A. Hyperparameters for ASPConvs 1, 2

Each block consists of three layers of an ASP layer, a convolution layer, and a rectified linear unit (ReLU) activation function. In Block ASPConv 1, for the ASP layer, the kernel contains 3×3 nonzero weights, 128 filters, stride = 1, and padding = same. For the convolution layer, there are 128 filter kernels of size 1×1 , stride = 2, and padding = same. After the convolution operation, ReLU activation functions are followed. As a practice, a padding operation is conducted to ensure that the feature maps remain the same size before and after convolutions. In ASPConv 2, for the ASP layer, the kernel contains 3×3 nonzero weights, 256 filters, stride = 1, and padding = same. For the convolution layer, the kernel contains 1×1 nonzero weights, 256 filters, stride = 2, and padding = same. After the convolution operation, the ReLU activation functions and batch normalization (BN) layers are followed.

B. Hyperparameters for ASPCaps 1, 2

There are two ASPC blocks. For ASPCaps 1, the kernel contains 3×3 nonzero weights, 32×4 filters, stride = 1, and padding = same. After the ASPC operation, ReLU activation functions are followed. For ASPCaps 2, the kernel contains 3×3 nonzero weights, 32×4 filters, stride = 1, and padding = same.

REFERENCES

- [1] B. Du, Y. Zhang, L. Zhang, and D. Tao, "Beyond the sparsity-based target detector: A hybrid sparsity and statistics-based detector for hyperspectral images," *IEEE Trans. Image Process.*, vol. 25, no. 11, pp. 5345–5357, 2016.
- [2] R. Qureshi, M. Uzair, K. Khurshid, and H. Yan, "Hyperspectral document image processing: Applications, challenges and future prospects," *Pattern Recognit.*, vol. 90, pp. 12–22, 2019.
- [3] X.-H. Han, Y. Zheng, J. Sun, and Y.-W. Chen, "Hyperspectral reconstruction with redundant camera spectral sensitivity functions," *ACM Trans. Multimedia Comput. Commun. Appl.*, vol. 16, no. 2, pp. 1–15, 2020.
- [4] L. Wang, M. Jia, D. Yin, and J. Tian, "A review of remote sensing for mangrove forests: 1956–2018," *Remote Sens. Environment*, vol. 231, pp. 1–15, 2019.
- [5] C.-C. Liu, T.-W. Hsu, H.-L. Wen, and K.-H. Wang, "Mapping pure mangrove patches in small corridors and sandbanks using airborne hyperspectral imagery," *Remote Sens.*, vol. 11, no. 5, p. 592, 2019.
- [6] F. Melgani and L. Bruzzone, "Classification of hyperspectral remote sensing images with support vector machines," *IEEE Trans. Geosci. Remote Sens.*, vol. 42, no. 8, pp. 1778–1790, 2004.
- [7] J. Li, J. M. Bioucas-Dias, and A. Plaza, "Spectral–spatial hyperspectral image segmentation using subspace multinomial logistic regression and markov random fields," *IEEE Trans. Geosci. Remote Sens.*, vol. 50, no. 3, pp. 809–823, 2011.
- [8] P. Ghamisi, J. Plaza, Y. Chen, J. Li, and A. J. Plaza, "Advanced spectral classifiers for hyperspectral images: A review," *IEEE Geosci. Remote Sens. Magazine*, vol. 5, no. 1, pp. 8–32, 2017.
- [9] L. Ma, Y. Liu, X. Zhang, Y. Ye, G. Yin, and B. A. Johnson, "Deep learning in remote sensing applications: A meta-analysis and review," *ISPRS J. Photogrammetry Remote Sens.*, vol. 152, pp. 166–177, 2019.
- [10] K. Tan, H. Wang, L. Chen, Q. Du, P. Du, and C. Pan, "Estimation of the spatial distribution of heavy metal in agricultural soils using airborne hyperspectral imaging and random forest," *J. Hazardous Mater.*, vol. 382, p. 120987, 2020.
- [11] M. Dalponte, H. O. Ørka, T. Gobakken, D. Gianelle, and E. Næsset, "Tree species classification in boreal forests with hyperspectral data," *IEEE Trans. Geosci. Remote Sens.*, vol. 51, no. 5, pp. 2632–2645, 2013.
- [12] Y. Gu, T. Liu, X. Jia, J. A. Benediktsson, and J. Chanussot, "Nonlinear multiple kernel learning with multiple-structure-element extended morphological profiles for hyperspectral image classification," *IEEE Trans. Geosci. Remote Sens.*, vol. 54, no. 6, pp. 3235–3247, 2016.
- [13] P. Ghamisi, J. A. Benediktsson, and M. O. Ulfarsson, "Spectral–spatial classification of hyperspectral images based on hidden markov random fields," *IEEE Trans. Geosci. Remote Sens.*, vol. 52, no. 5, pp. 2565–2574, 2014.
- [14] B. Tu, X. Zhang, X. Kang, G. Zhang, J. Wang, and J. Wu, "Hyperspectral image classification via fusing correlation coefficient and joint sparse representation," *IEEE Geosci. Remote Sens. Lett.*, vol. 15, no. 3, pp. 340–344, 2018.
- [15] Y. Chen, N. M. Nasrabadi, and T. D. Tran, "Hyperspectral image classification using dictionary-based sparse representation," *IEEE Trans. Geosci. Remote Sens.*, vol. 49, no. 10, pp. 3973–3985, 2011.
- [16] L. Fang, C. Wang, S. Li, and J. A. Benediktsson, "Hyperspectral image classification via multiple-feature-based adaptive sparse representation," *IEEE Trans. Instrum. Meas.*, vol. 66, no. 7, pp. 1646–1657, 2017.
- [17] C. Cao, L. Deng, W. Duan, F. Xiao, W. Yang, and K. Hu, "Hyperspectral image classification via compact-dictionary-based sparse representation," *Multimed. Tools. Appl.*, vol. 78, no. 11, pp. 15 011–15 031, 2019.
- [18] L. He, J. Li, C. Liu, and S. Li, "Recent advances on spectral–spatial hyperspectral image classification: An overview and new guidelines," *IEEE Trans. Geosci. Remote Sens.*, vol. 56, no. 3, pp. 1579–1597, 2017.
- [19] X. Kang, S. Li, and J. A. Benediktsson, "Feature extraction of hyperspectral images with image fusion and recursive filtering," *IEEE Trans. Geosci. Remote Sens.*, vol. 52, no. 6, pp. 3742–3752, 2014.
- [20] J. A. Benediktsson, J. A. Palmason, and J. R. Sveinsson, "Classification of hyperspectral data from urban areas based on extended morphological profiles," *IEEE Trans. Geosci. Remote Sens.*, vol. 43, no. 3, pp. 480–491, 2005.
- [21] X. Kang, S. Li, and J. A. Benediktsson, "Spectral–spatial hyperspectral image classification with edge-preserving filtering," *IEEE Trans. Geosci. Remote Sens.*, vol. 52, no. 5, pp. 2666–2677, 2014.
- [22] X. Tu, X. Shen, P. Fu, T. Wang, Q. Sun, and Z. Ji, "Discriminant subdictionary learning with adaptive multiscale superpixel representation for hyperspectral image classification," *Neurocomputing*, vol. 409, pp. 131–145, 2020.
- [23] B. Tu, J. Wang, X. Kang, G. Zhang, X. Ou, and L. Guo, "Knn-based representation of superpixels for hyperspectral image classification," *IEEE J. Sel. Topics Appl. Earth Observ. Remote Sens.*, vol. 11, no. 11, pp. 4032–4047, 2018.
- [24] A. Bordes, X. Glorot, J. Weston, and Y. Bengio, "Joint learning of words and meaning representations for open-text semantic parsing," in *Proc. Int. Conf. Artificial Intell. Statist.* PMLR, 2012, pp. 127–135.
- [25] R. Girshick, J. Donahue, T. Darrell, and J. Malik, "Rich feature hierarchies for accurate object detection and semantic segmentation," in *Proc. IEEE Conf. Comput. Vis. Pattern Recognit. (CVPR)*, Jun. 2014.
- [26] J. Redmon, S. Divvala, R. Girshick, and A. Farhadi, "You only look once: Unified, real-time object detection," in *Proc. IEEE Conf. Comput. Vis. Pattern Recognit. (CVPR)*, Jun. 2016.
- [27] J. Ma, H. Zhang, P. Liang, and H. Xu, "Ganmcc: A generative adversarial network with multi-classification constraints for infrared and visible image fusion," *IEEE Trans. Instrum. Meas.*, 2020, In Press.
- [28] C. Szegedy, W. Liu, Y. Jia, P. Sermanet, S. Reed, D. Anguelov, D. Erhan, V. Vanhoucke, and A. Rabinovich, "Going deeper with convolutions," in *Proc. IEEE Conf. Comput. Vis. Pattern Recognit. (CVPR)*, Jun. 2015.
- [29] S. Li, W. Song, L. Fang, Y. Chen, P. Ghamisi, and J. A. Benediktsson, "Deep learning for hyperspectral image classification: An overview," *IEEE Trans. Geosci. Remote Sens.*, vol. 57, no. 9, pp. 6690–6709, 2019.
- [30] Y. Chen, Z. Lin, X. Zhao, G. Wang, and Y. Gu, "Deep learning-based classification of hyperspectral data," *IEEE J. Sel. Topics Appl. Earth Observ. Remote Sens.*, vol. 7, no. 6, pp. 2094–2107, 2014.
- [31] J. Yue, S. Mao, and M. Li, "A deep learning framework for hyperspectral image classification using spatial pyramid pooling," *Remote Sens. Lett.*, vol. 7, no. 9, pp. 875–884, 2016.
- [32] Y. Chen, X. Zhao, and X. Jia, "Spectral–spatial classification of hyperspectral data based on deep belief network," *IEEE J. Sel. Topics Appl. Earth Observ. Remote Sens.*, vol. 8, no. 6, pp. 2381–2392, 2015.

- [33] L. Mou, P. Ghamisi, and X. X. Zhu, "Deep recurrent neural networks for hyperspectral image classification," *IEEE Trans. Geosci. Remote Sens.*, vol. 55, no. 7, pp. 3639–3655, 2017.
- [34] I. Goodfellow, J. Pouget-Abadie, M. Mirza, B. Xu, D. Warde-Farley, S. Ozair, A. Courville, and Y. Bengio, "Generative adversarial nets," in *Proc. Int. Conf. Neural Inf. Process. Syst.*, 2014, pp. 2672–2680.
- [35] H. Lee and H. Kwon, "Going deeper with contextual cnn for hyperspectral image classification," *IEEE Trans. Image Process.*, vol. 26, no. 10, pp. 4843–4855, 2017.
- [36] W. Song, S. Li, L. Fang, and T. Lu, "Hyperspectral image classification with deep feature fusion network," *IEEE Trans. Geosci. Remote Sens.*, vol. 56, no. 6, pp. 3173–3184, 2018.
- [37] J. Yue, W. Zhao, S. Mao, and H. Liu, "Spectral–spatial classification of hyperspectral images using deep convolutional neural networks," *Remote Sens. Lett.*, vol. 6, no. 6, pp. 468–477, 2015.
- [38] B. Fang, Y. Li, H. Zhang, and J. C.-W. Chan, "Hyperspectral images classification based on dense convolutional networks with spectral-wise attention mechanism," *Remote Sens.*, vol. 11, no. 2, p. 159, 2019.
- [39] B. Pan, X. Xu, Z. Shi, N. Zhang, H. Luo, and X. Lan, "Dssnet: A simple dilated semantic segmentation network for hyperspectral imagery classification," *IEEE Geosci. Remote Sens. Lett.*, pp. 1–5, to be published, 2020.
- [40] R. R. Devaram, D. Allegra, G. Gallo, and F. Stanco, "Hyperspectral image classification via convolutional neural network based on dilation layers," in *Int. Conf. Image Analysis Process.* Springer, 2019, pp. 378–387.
- [41] K. Pooja, R. R. Nidamanuri, and D. Mishra, "Multi-scale dilated residual convolutional neural network for hyperspectral image classification," in *Proc. IEEE 10th Workshop Hyperspectral Imag. Signal Process., Evol. Remote Sens.*, 2019, pp. 1–5.
- [42] Y. Xu, B. Du, and L. Zhang, "Beyond the patchwise classification: Spectral-spatial fully convolutional networks for hyperspectral image classification," *IEEE Trans. Big Data*, vol. 6, no. 3, pp. 492–506, 2020.
- [43] X. Li, M. Ding, and A. Pižurica, "Deep feature fusion via two-stream convolutional neural network for hyperspectral image classification," *IEEE Trans. Geosci. Remote Sens.*, vol. 58, no. 4, pp. 2615–2629, 2020.
- [44] X.-H. Han, Y. Zheng, and Y.-W. Chen, "Multi-level and multi-scale spatial and spectral fusion cnn for hyperspectral image super-resolution," in *Proc. IEEE Int. Conf. Comput. Vis. (ICCV)*, 2019, pp. 4330–4339.
- [45] C. Mu, Z. Guo, and Y. Liu, "A multi-scale and multi-level spectral-spatial feature fusion network for hyperspectral image classification," *Remote Sens.*, vol. 12, no. 1, p. 125, 2020.
- [46] S. Sabour, N. Frosst, and G. E. Hinton, "Dynamic routing between capsules," in *Proc. Int. Conf. Neural Inf. Process. Syst.*, 2017, pp. 3856–3866.
- [47] M. E. Paoletti, J. M. Haut, R. Fernandez-Beltran, J. Plaza, A. Plaza, J. Li, and F. Pla, "Capsule networks for hyperspectral image classification," *IEEE Trans. Geosci. Remote Sens.*, vol. 57, no. 4, pp. 2145–2160, 2018.
- [48] J. Rajasegaran, V. Jayasundara, S. Jayasekara, H. Jayasekara, S. Seneviratne, and R. Rodrigo, "Deepcaps: Going deeper with capsule networks," in *Proc. IEEE Conf. Comput. Vis. Pattern Recognit.*, 2019, pp. 10725–10733.
- [49] P. Arun, K. M. Buddhiraju, and A. Porwal, "Capsulenet-based spatial-spectral classifier for hyperspectral images," *IEEE J. Sel. Topics Appl. Earth Observ. Remote Sens.*, vol. 12, no. 6, pp. 1849–1865, 2019.
- [50] K. Zhu, Y. Chen, P. Ghamisi, X. Jia, and J. A. Benediktsson, "Deep convolutional capsule network for hyperspectral image spectral and spectral-spatial classification," *Remote Sens.*, vol. 11, no. 3, p. 223, 2019.
- [51] W. Zhang, P. Tang, and L. Zhao, "Remote sensing image scene classification using cnn-capsnet," *Remote Sens.*, vol. 11, no. 5, p. 494, 2019.
- [52] Q. Xu, D. Y. Wang, and B. Luo, "Faster multiscale capsule network with octave convolution for hyperspectral image classification," *IEEE Geosci. Remote Sens. Lett.*, 2020.
- [53] W. Li, G. Wu, F. Zhang, and Q. Du, "Hyperspectral image classification using deep pixel-pair features," *IEEE Trans. Geosci. Remote Sens.*, vol. 55, no. 2, pp. 844–853, 2016.
- [54] Y. Li, L. Zhang, C. Ding, W. Wei, and Y. Zhang, "Single hyperspectral image super-resolution with grouped deep recursive residual network," in *Proc. IEEE 4th Int. Conf. Multimedia Big Data (BigMM)*. IEEE, 2018, pp. 1–4.
- [55] X. Li, M. Ding, and A. Pižurica, "Group convolutional neural networks for hyperspectral image classification," in *IEEE Int. Conf. Image Process. (ICIP)*, 2019, pp. 639–643.
- [56] J. Dai, H. Qi, Y. Xiong, Y. Li, G. Zhang, H. Hu, and Y. Wei, "Deformable convolutional networks," in *Proc. IEEE Int. Conf. Comput. Vis. (ICCV)*, Oct. 2017.
- [57] X. Zhu, H. Hu, S. Lin, and J. Dai, "Deformable convnets v2: More deformable, better results," in *Proc. IEEE Conf. Comput. Vis. Pattern Recognit. (CVPR)*, Jun. 2019.
- [58] J. Zhu, L. Fang, and P. Ghamisi, "Deformable convolutional neural networks for hyperspectral image classification," *IEEE Geosci. Remote Sens. Lett.*, vol. 15, no. 8, pp. 1254–1258, 2018.
- [59] C. Xiang, L. Zhang, Y. Tang, W. Zou, and C. Xu, "Ms-capsnet: A novel multi-scale capsule network," *IEEE Signal Process. Lett.*, vol. 25, no. 12, pp. 1850–1854, 2018.
- [60] C. Xiang, Z. Wang, S. Tian, J. Liao, W. Zou, and C. Xu, "Matrix capsule convolutional projection for deep feature learning," *IEEE Signal Process. Lett.*, 2020.
- [61] P. Wang, P. Chen, Y. Yuan, D. Liu, Z. Huang, X. Hou, and G. Cottrell, "Understanding convolution for semantic segmentation," in *Proc. Winter Conf. Appl. Comput. Vis. (WACV)*. IEEE, 2018, pp. 1451–1460.
- [62] R. Moreno, F. Corona, A. Lendasse, M. Graña, and L. S. Galvão, "Extreme learning machines for soybean classification in remote sensing hyperspectral images," *Neurocomputing*, vol. 128, pp. 207–216, 2014.